Supporting Information

Fraser et al. 10.1073/pnas.1111325108

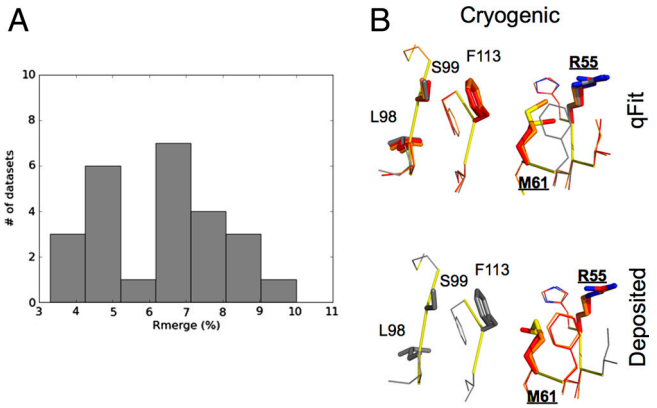

Fig. S1. R_{merge} values and qFit enable comparisons of cryogenic and room-temperature datasets. (*A*) A histogram of published Rmerge values for room-temperature datasets indicate that no unusual radiation damage has occurred. All values are below 10% across the entire resolution range. We do not observe widespread effects of radiation damage, such as S oxidation, scission of disulfide bonds, or opening of aromatic rings. Below, we have compiled a list of specific references to the procedures used by the individual investigators to limit radiation damage: *Cyclophilin*: "Room-temperature X-ray data were collected at 15 °C with 96% humidity using a temperature- and humidity-controlled goniometer head (the Rigaku free-mounting device) at ALS Beamline 12.3.1. To limit the effects of radiation damage while maintaining high signal-to-noise, we collected short exposures (0.1 s) for 180 degrees with 1 degree oscillations. A large crystal (1 mm × 0.5 mm × 0.3 mm) was translated halfway through this rapid collection protocol. Following this initial low-exposure pass, an additional complete dataset of 90 degrees with longer exposures (1 s) was collected while translating the crystal every 10 frames. During data processing, we ensured that radiation damage had not degraded the data quality by subdividing the data into subsets of 45 frames and confirming that unit cell parameters, scale factors, and chi-square statistics were consistent throughout the dataset. Owing to the short total exposure time (108 s), the limited exposure of each spot on the crystal, the size of the crystal, and the finite rate of crystal damage, the data were not significantly influenced by radiation damage." (1). *Crystallin*: "A two degree oscillation range was used and the crystal was translated through the beam roughly every 20 degrees in order to minimize radiation damage." (2). *Pilin*: "To obtain the final dataset, scaling and merging were carried out in a non-standard manner. Firstly, batch 1 was scaled and merged separately. Next all four batches were processed together and scaled to batch 1. Finally, the program SFTOOLS was used to create the missing reflections from the scaled set of all data. This minimized the effect of radiation damage without compromising the data completeness" (3). *RNAse T1*: "Their intensities were corrected for crystal decay, which did not exceed 9%" (4). *Rubredoxin*: "Each frame consisted of a 1 degree oscillation with .5 s exposure time. To counter the heating effect of the X-ray beam, the beam was attenuated to 25% of full strength and a 295 K gas stream was flowed over the crystal." (5). *Xylanase*: "To cover the whole range of intensities, three sets of images were recorded, differing in exposure times and resolution limits, for the cryodata and two sets of images were recorded for the room-temperature data." (6). (*B*) Model building and refinement of CypA using qFit shows that the cryogenic X-ray data reveal a single conformation for many residues (Leu98, Ser99 and Phe113) that agree with the deposited model.

1 Fraser JS, et al. (2009) Hidden alternative structures of proline isomerase essential for catalysis. *Nature* 462:669–673.
2 Najmudin, et al. (1993) Structure of the bovine eye lens protein gammaB(gammaII)-crystallin at 1.47 A. *Acta Crystallogr D Biol Crystallogr* 49:223–233.
3 Dunlop, et al. (2005) Pros and cons of cryocrystallography: Should we also collect a room-temperature data set? *Acta Crystallogr D Biol Crystallogr* 61:80–87.
4 Martinez-Oyanedel, et al. (1991) Ribonuclease T1 with free recognition and catalytic site: Crystal structure analysis at 1.5 A resolution. *J Mol Biol* 222:335–352.
5 Gardberg AS, et al. (2010) Unambiguous determination of H-atom positions: Comparing results from neutron and high-resolution X-ray crystallography. *Acta Crystallogr D Biol Crystallogr* 66:558–567.
6 Natesh, et al. (2003) Thermostable xylanase from *Thermoascus aurantiacus* at ultrahigh resolution (0.89 A) at 100 K and atomic resolution (1.11 A) at 293 K refined anisotropically to small-molecule accuracy. *Acta Crystallogr D Biol Crystallogr* 59:105–117.

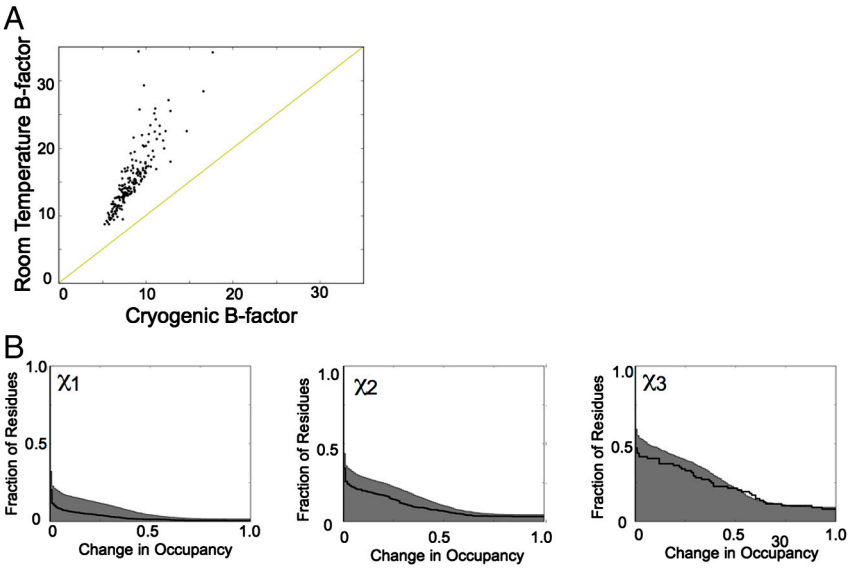

Fig. S2. Changes in B-factors and rotamers induced by crystal cryocooling. (*A*) A scatter plot of residue-averaged B-factors for cryogenic and room-temperature xylanase II. Although crystal cryocooling causes only modest structural effects on the overall folds of all 30 proteins, the average atomic B-factors are reduced and the B-factor distributions are narrowed compared to models refined against isomorphous room-temperature data. Residues that deviate from predicted linear reductions in B-factors may reflect local variations in effective temperature, differential coupling to the solvent or the lattice, or changes in the relative populations of alternative conformations. Rather than directly modeling the populations of interconverting alternative conformations, the B-factors approximate local harmonic displacements. All residues fall above the yellow equality line, which indicates that B-factors capture increased thermal motion at room temperature. (*B*) Cumulative histograms of the maximum absolute change in rotamer occupancy from qFit models for all residues (shaded gray area) and buried residues (black line) reveal that cryocooling affects the conformational substates at multiple χ-angles.

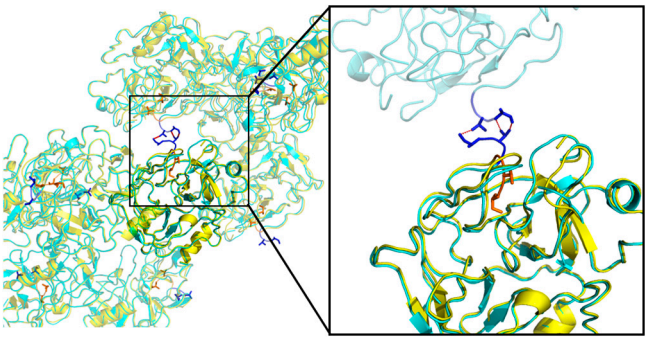

Fig. S3. A functionally important loop in trypsinogen forms new lattice contacts upon crystal cryocooling. In trypsinogen, which has the largest rmsd of any structure pair in our dataset (1.1 Å), cryocooling induces a conformational change in the N-terminal terminal loop. The room-temperature (yellow) and cryogenic (cyan) models of trypsinogen are shown in the crystal lattice environment. The inset focuses on the N-terminal loop, which adopts a buried conformation at room temperature (yellow/orange). In contrast, at cryogenic temperatures, the loop adopts an exposed conformation and forms new symmetric side-chain lattice contacts (red dashes) in a solvent channel. This loop is flexible in solution and is important for the proteolytic maturation into trypsin. Trypsinogen provides a dramatic example of how cooling causes small but significant structural changes and the formation of additional lattice contacts. The differences between the room-temperature and cryogenic structures of trypsinogen highlight functionally important flexible residues that are mobile in solution.

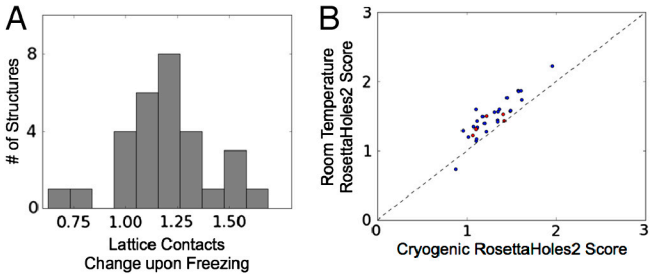

Fig. S4. Cryocooling changes lattice contacts and protein packing. (*A*) A histogram of the change in lattice contacts indicates that cryocooling increases lattice contacts. Lattices with increased contacts (cryogenic/room-temperature ratio >1.0) may help to stabilize the arrangement of proteins in the crystal, leading to increases in resolution at cryogenic temperatures. (*B*) RossetaHoles2 packing score for room-temperature vs. cryogenic models. Lower scores indicate better packing. All pairs of refined models, except partially deuterated rubridoxin, show quantitatively superior packing at cryogenic temperatures. Proteins where the room-temperature dataset is higher resolution are shown in red.

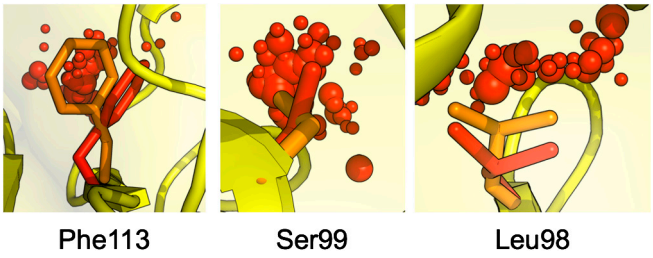

Fig. S5. The association of packing defects and alternative conformations. Packing defects (red spheres) are partially filled by nearby alterative conformations (orange) of Phe113, Ser99, and Leu98 in CypA. Only the major conformations (red) are detectable by Ringer or qFit at cryogenic temperatures, where these packing defects are absent.

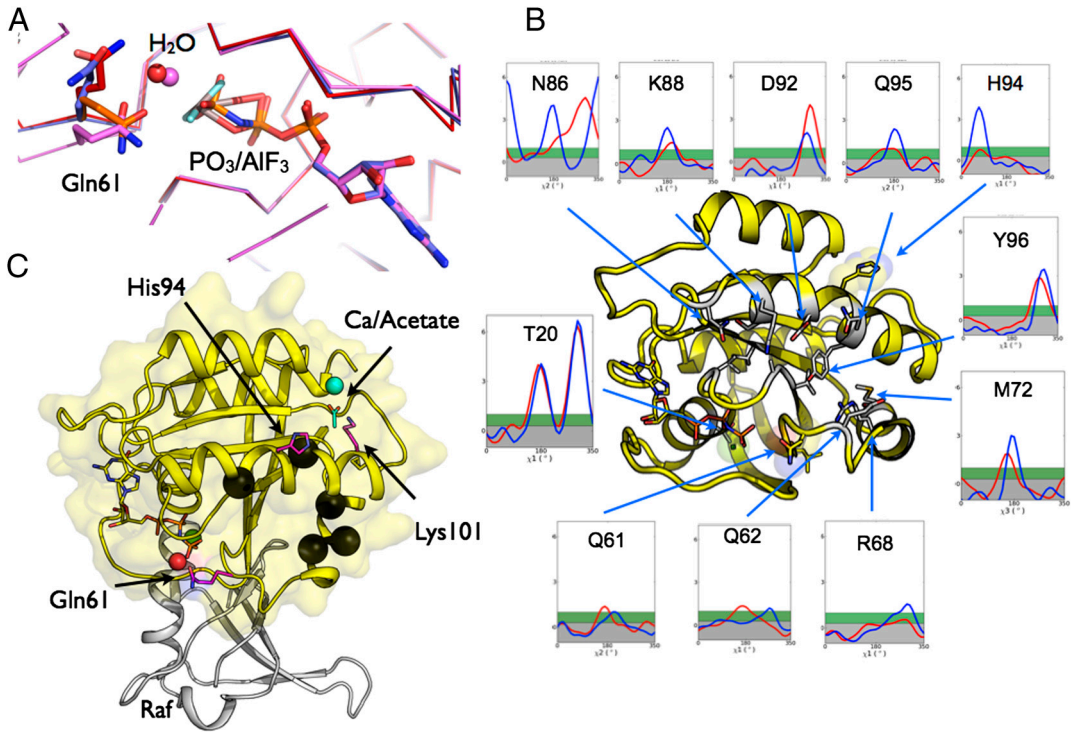

Fig. S6. Temperature dependence of the H-Ras:GTP allosteric mechanism. (*A*) Substrate-based superposition of H-Ras cryogenic (blue), room-temperature (red and orange), and transition state (violet) models (as in Fig. 5*B*). (*B*) The room-temperature qFit model and Ringer plots link helix 3 residues to the catalytically competent active site by temperature-dependent changes in conformational distributions. (*C*) Perturbations to the dynamic network, which extends from the cavity at the C-terminal end of helix 3 to the active site, identified by relaxation dispersion NMR in H-Ras and room-temperature electron-density sampling, can cause long-range changes in the conformational ensemble and activity of H-Ras. However, each perturbation selects from the ensemble different conformations with distinct functional properties. Recent X-ray studies have revealed that binding of Ca^{2+} and acetate (shown in cyan, upper right) in the allosteric cavity modulates the conformational ensemble (from PDB ID code 3LBH). Although Ca^{2+} is not known to directly regulate H-Ras, Ca^{2+} binding in the crystal prevents collapse of the cavity, selects alternative side-chain conformations along helix 3, and stabilizes the catalytically competent conformation of Gln61 (shown in pink lower left). The key residues implicated in this conformational change match flexible residues identified in the absence of Ca^{2+} both by NMR relaxation and by our analysis of the room-temperature ensemble. Mutation of Lys101 (shown in pink) near the allosteric cavity alters the morphological outcome of interactions between Raf (shown in gray from PDB ID code 3KUD) and the Ras active site, including Gln61 (shown in pink). Mutations identified in cancers are shown as black spheres adjacent to helix 3 and His94 (shown in pink).

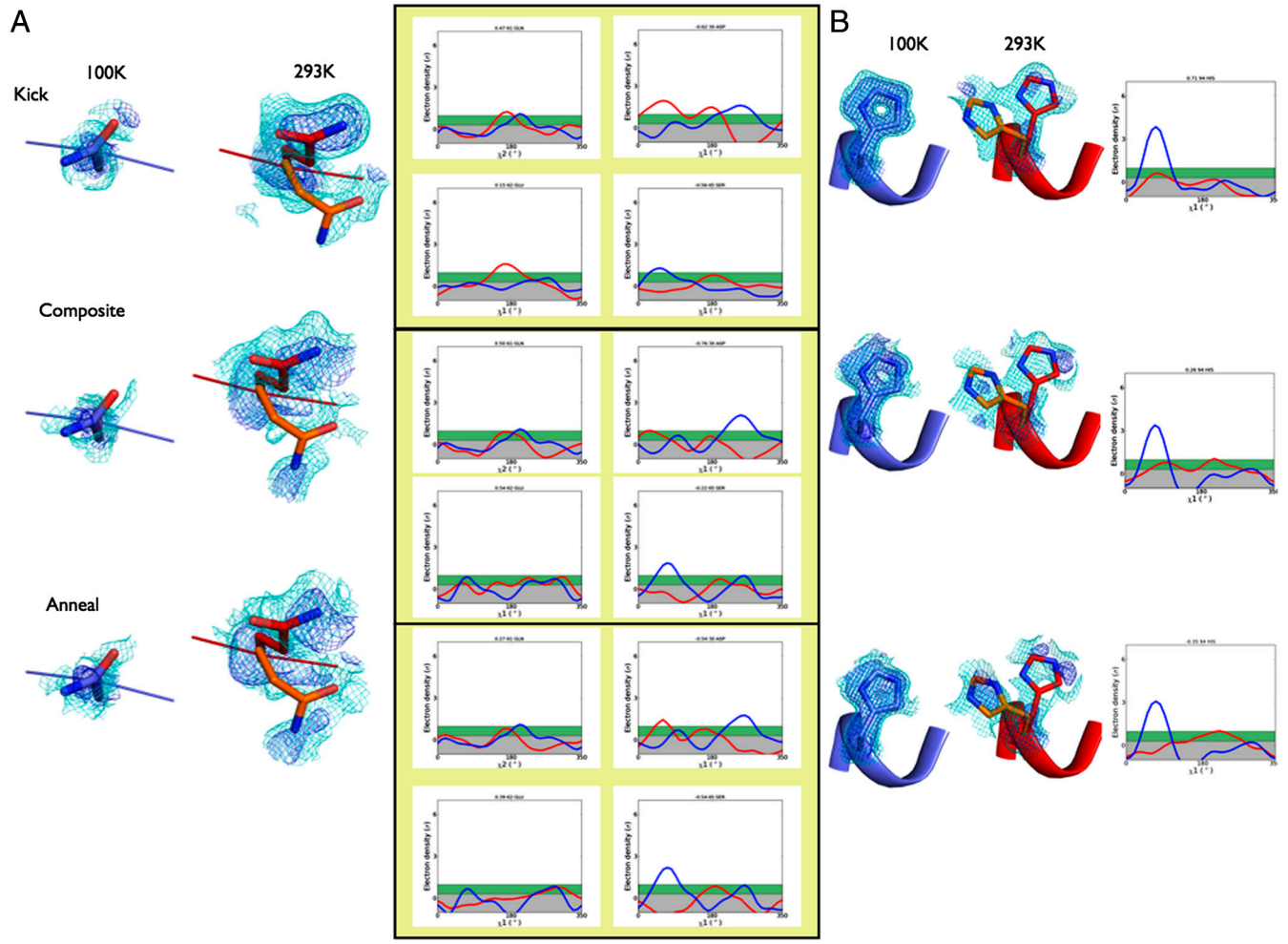

Fig. S7. Minor populations are detected in different types of electron-density maps. (*A*) A comparison of Phenix-kicked, composite-omit, and simulated-annealing omit maps for the active site residues of H-Ras reveals electron density consistent with a second conformation of Gln61. Electron-density distributions reveal differences between the room-temperature and cryogenic maps in these map types, consistent with the interpretations made using maximum-likelihood weighted maps. The reduction in the −60° peak of Gln61 at $\chi 2$ is due to a coupled backbone/side-chain shift that places the peak corresponding to the alternative Cδ position outside the sampling radius of Ringer. (*B*) Different electron-density maps for His94 of H-Ras reveal features consistent with a second conformation at room temperature. Ringer plots reveal differences between the room-temperature and cryogenic maps in all three map types, consistent with the interpretations made using maximum-likelihood weighted maps. The differences in the H-Ras active site could be due to factors other than temperature (for example, a "bad dataset"). However, there are several considerations that argue against this possibility. The cryogenic model refined well (Table S1), and the map is of very high quality in other regions, for example His94. Analysis of the reflections by phenix.xtriage indicates no indicators of dataset pathologies such as: twinning, ice-rings, or anisotropy. This suggests that the difficulty in interpreting the Gln61 area is not a property of the crystal or the data quality but rather stems from the cryogenic procedure. The room-temperature map, in contrast, can be interpreted as exchanging between the "active" and "inactive" conformation. While the cryogenic data are best interpreted as a single conformation with high B-factors, the room-temperature electron-density maps reveal multiple conformations with different potential activities. This difference suggests that cryogenic artifacts may complicate the interpretation of biological mechanisms in weak electron density.

Table S1. Matched structures determined at cryogenic and room temperatures

Table S1	Room Temperature					Cryogenic Temperature				
Protein	ID	Resolution (Å)	R/Rfree (Deposited)	R/Rfree (Refined)	R/Rfree (qFit)	ID	Resolution (Å)	R/Rfree (Deposited)	R/Rfree (Refined)	R/Rfree (qFit)
alkaline protease	1wme	1.50	12.6/16.6	10.1/13.6	9.98/13.4	1wmd	1.30	13.4/16.9	12.4/15.2	12.3/15.4
asparaginase	2wt4	1.80	15.3/18.5	14.0/17.4	13.7/17.4	2wlt	1.40	13.1/16.9	12.4/15.8	12.4/16.1
barnase	1a2p	1.50	11.1/17.4	11.2/15.5	11.0/15.5	1b2x	1.80	17.3/23.6	15.6/19.1	15.3/19.9
bpti:trypsin	3btk	1.85	20.2/23.0	16.5/19.3	15.9/19.1	2ftl	1.62	21.5/22.7	13.4/17.5	14.4/19.3
co-myoglobin	1bzr	1.15	12.4/-	12.8/15.2	12.8/15.9	1a6g	1.15	12.7/16.0	14.0/15.9	14.6/17.3
crambin	1jxu	0.99	9.0/-	10.3/14.8	10.9/16.2	1jxt	0.89	14.5/-	12.4/14.0	12.0/13.8
crystallin	4gcr	1.47	18.1/-	12.8/19.4	12.5/19.9	1gcs	2.00	17.0/-	17.1/20.1	14.3/19.4
cypa-s99t	3k0o	1.55	11.1/14.8	10.7/14.9	10.1/15.1	3k0p	1.65	15.0/17.6	15.5/17.7	15.6/18.0
cypa-wt	3k0n	1.39	12.4/16.0	11.8/15.2	11.6/15.0	3k0m	1.25	13.1/14.9	12.7/14.5	12.6/14.2
deoxy-myoglobin	1bzp	1.15	11.4/-	12.6/15.1	12.7/16.3	1a6n	1.15	12.1/14.5	13.8/16.4	13.9/16.1
ferredoxin	1fdn	1.84	16.9/-	12.7/15.2	12.0/14.5	2fdn	0.94	10.0/-	11.1/12.2	11.4/12.8
glutathione reductase	3djg	1.80	14.5/18.6	16.4/19.5	15.4/19.1	3djj	1.10	11.3/14.7	12.6/13.7	12.4/14.4
hen lysozyme	4lzt	0.95	11.4/14.7	11.6/12.6	11.3/12.7	3lzt	0.93	9.3/11.4	11.2/12.5	11.0/12.3
hirustasin	1bx8	1.40	17.7/20.7	13.1/17.8	13.2/18.9	1bx7	1.20	17.9/22.5	15.1/19.4	14.1/19.0
met-myoglobin	1bz6	1.20	9.1/-	10.2/12.3	10.4/13.2	1a6k	1.10	13.1/15.3	13.2/14.9	13.1/15.2
pilin	1x6p	1.63	14.1/15.8	14.9/17.1	14.3/17.2	1x6q	1.51	13.9/16.1	12.7/19.3	13.1/20.4
plastocyanin	1plc	1.33	15.0/-	11.5/17.1	11.1/17.5	1pnc	1.60	13.2/-	13.9/17.9	13.5/18.3
rnase sa	1rgg	1.20	10.6/-	11.6/13.8	11.2/14.1	1lni	1.00	11.6/-	13.5/15.5	13.8/16.3
rnase t1	9rnt	1.50	14.3/-	10.7/18.1	11.3/16.8	1i0v	1.23	17.9/19.2	11.4/14.5	11.1/14.4
rubredoxin	3kyw	1.10	15.3/16.5	13.8/14.6	13.2/15.1	3kyv	1.10	12.9/14.7	12.6/14.3	12.2/14.1
superoxide dismutase	2jcw	1.70	19.1/-	15.1/16.8	14.7/16.3	1jcv	1.55	19.0/-	13.3/17.4	13.4/17.9
superoxide reductase*	1do6	2.00	16.2/18.9	14.9/17.7	13.9/17.8	1dqi	1.70	20.4/21.7	17.5/19.5	16.6/19.4
thaumatin	1kwn	1.20	12.7/14.5	11.1/12.2	11.0/12.7	1ly0	1.36	19.6/20.4	12.5/15.1	11.8/14.9
trypsinogen	1tgc	1.80	-/-	15.4/18.7	14.4/19.2	1tgt	1.70	18.7/-	17.2/19.9	16.0/20.8
trypsin	1gdu	1.07	10.4/-	11.6/13.7	11.4/14.5	1gdq	0.93	9.9/-	12.2/13.8	11.9/13.4
xylanase	1i1x	1.11	9.9/12.4	10.4/12.4	10.3/12.8	1i1w	0.89	9.0/10.6	10.9/11.5	10.7/11.5
xylanase II	2dfc	1.19	10.6/12.2	12.0/13.0	11.9/13.0	2dfb	1.11	10.8/12.1	13.5/14.9	13.6/15.1
t4 lysozyme	1l63	1.75	14.8/-	16.1/17.9	15.9/18.0	1lw9	1.45	20.0/25.4	15.4/19.8	15.8/20.2
t4 lysozyme-l99a	1l90	1.75	15.6/-	16.4/20.0	16.6/20.4	3dmv	1.65	18.4/21.0	16.7/20.0	16.2/19.6
ras	3TGP	1.31	-/-	-/-	14.5/21.7	1ctq	1.26	17.2/22.4	13.6/18.2	12.7/18.3

Note: "-" indicates that a model or Rfree statistic was not deposited in the PDB; "*" excluded from volume calculations due to differences in *c*-axis.